Competition between drag and Coulomb interactions in turbulent particle-laden flows using a coupled-fluid–Ewald-summation based approach

Yuan Yao* and Jesse Capecelatro
Department of Mechanical Engineering, University of Michigan, Ann Arbor, Michigan 48105, USA

(Received 8 September 2017; published 6 March 2018)

We present a numerical study on inertial electrically charged particles suspended in a turbulent carrier phase. Fluid-particle interactions are accounted for in an Eulerian-Lagrangian (EL) framework and coupled to a Fourier-based Ewald summation method, referred to as the particle-particle-particle–mesh (P^3M) method, to accurately capture short- and long-range electrostatic forces in a tractable manner. The EL P^3M method is used to assess the competition between drag and Coulomb forces for a range of Stokes numbers and charge densities. Simulations of like- and oppositely charged particles suspended in a two-dimensional Taylor-Green vortex and three-dimensional homogeneous isotropic turbulence are reported. It is found that even in dilute suspensions, the short-range electric potential plays an important role in flows that admit preferential concentration. Suspensions of oppositely charged particles are observed to agglomerate in the form of chains and rings. Comparisons between the particle-mesh method typically employed in fluid-particle calculations and P^3M are reported, in addition to one-point and two-point statistics to quantify the level of clustering as a function of Reynolds number, Stokes number, and nondimensional electric settling velocity.

DOI: 10.1103/PhysRevFluids.3.034301

I. INTRODUCTION

Nontrivial interactions between electrically charged particles and turbulence play an important role in many engineering and environmental flows, including atmospheric clouds [1], fluidized bed reactors [2–4], charged hydrocarbon sprays [5–7], dusty plasmas [8,9], and wind-blown dust [9,10]. Throughout the atmosphere, for example, ion pairs are produced by cosmic rays that attach to aerosol particles and droplets. Ionization of atmospheric air together with the potential difference that exists between the upper atmosphere and the earth's surface generates a non-negligible vertical electric field that can potentially affect the collision rate and coalescence between charged droplets, which dictates the onset of rainfall [1]. Dilute suspensions of inertial (heavy) particles in isotropic turbulence will preferentially concentrate in regions of high strain rate and low vorticity [11]. Such coupling between particles and the underlying carrier phase can lead to significant spatial segregation in charge density that induces, or amplifies, an electric field. A recent study of the Sahara desert showed that electric fields contribute to an increase of up to ten times the amount of particles emitted into the atmosphere [10]. A positive feedback was observed whereby the electric field increases shear-induced dust lifting, which in turn introduces increased charges to the atmosphere resulting in a stronger electric field [9]. Meanwhile, the relative importance between fluid forces (i.e., drag) and electrostatic forces in turbulent flows remains elusive. When fluid-particle coupling is dominant, we expect the particles to preferentially concentrate in high-strain-rate regions of the flow, with the level of clustering determined by the Reynolds number and Stokes number [12]. With increasing charge magnitude,

*yyaoaa@umich.edu

eventually Coulomb interactions will have an order-one effect on the spatial distribution of particles. Thus, the primary interest of the current work is to investigate the competition between drag and Coulomb interactions on the particle distribution and to determine to what extent particles segregate as a function of the Reynolds number, Stokes number, and charge magnitude.

Numerical simulations can provide the space-time information needed to shed light on the complex interactions that occur in turbulent suspensions of electrically charged particles. Fluid-particle flows are commonly solved in either an Euler-Euler or Euler-Lagrange (EL) framework. Euler-Euler methods solve both the fluid and particle phase on a common Eulerian grid. In the small-Knudsen-number (highly collisional) limit with an underlying assumption that the flow is nearly at equilibrium, the particle velocity distribution is close to Maxwellian and a Chapman-Enskog expansion can be used to derive a two-fluid model (TFM) using ensemble or volume averaging [13–15]. This approach leads to particle-phase transport equations that closely resemble the Navier-Stokes equations using moment closures obtained from kinetic theory. While electrostatic models have been coupled with a TFM in the past [3,4], it is typically only valid in dense granular regimes and are unable to capture important features of particulate flows when the particle phase is far from equilibrium [16].

Euler-Lagrange methods provide an alternative framework that explicitly captures particle-particle interactions (e.g., collisions, short- and long-range interactions, etc.). In this approach, each particle is tracked individually and coupled to the fluid via interphase exchange terms [17,18]. Due to the long-range nature of electrostatic forces, however, properly accounting for Coulomb interactions in systems with many particles must be handled carefully for accurate predictions that avoid $O(N^2)$ computations, with N the number of charged particles. The particle-mesh (PM) method is typically employed in EL simulations (see, e.g., [19]) as it avoids computing direct pairwise sums. Instead, the charge is projected on the computational grid and the electric potential is solved via a Poisson equation. This method implicitly assumes that the electrostatic force between neighboring particles is small compared to the effect of all the particles combined. While computationally efficient, the PM method fails to capture short-range interactions that are anticipated to be important when particles cluster. An alternative approach is to apply a screen function, or cutoff radius, such that a limited range of particle interactions is considered and the far-field influence is ignored (see, e.g., [20]). In order to limit the computational burden, Lu and Shaw [20] summed the Coulomb contribution of all particles within the Debye screening radius. Such a truncated method is only valid for relatively low levels of clustering and small values of charge and is not applicable to particle-laden flows in general.

Ewald summations methods were developed to handle long-range potentials accurately in periodic boxes. This approach splits the slowly converging Coulomb potential into long-range and short-range contributions, each of which converges exponentially fast [21,22]. The short-range potential is evaluated using direct pairwise sums over the set of nearest neighbors within a cutoff radius and the long-range contribution is solved in reciprocal space. However, this approach remains computationally demanding as the long-range contribution requires several Fourier transforms and the total scheme scales like $O(N^{3/2})$ with an optimized cutoff radius [23,24]. The particle-particle-particle–mesh (P^3M) method introduced by Hockney and Eastwood [25] is a Fourier-based Ewald summation approach that makes use of an underlying grid to speed up the evaluation of the long-range potential. The P^3M method requires modifying the long-range potential in Fourier space to avoid double counting the short-range and long-range contributions and scales with $O(N \log N)$. The P^3M method has been applied to simulations of ionic liquids [26], molecular dynamics [27–29], and cosmology [30], yet to date has not been applied to particle-laden flows.

Based on these ideas, Kolehmainen *et al.* [31] recently proposed a method that computes the short-range force using a direct truncated pairwise summation approach and evaluates the cell-centered long-range force using a finite-volume method. As with the P^3M method, this method scales like $O(N \log N)$. Unlike Ewald summation methods, this approach (referred to herein as the hybrid method) is not restricted to periodic domains. However, the double-counting term is not computed as precisely as the P^3M, which impacts the overall accuracy of the scheme.

In the present study, the P^3M method is implemented within an Eulerian-Lagrangian framework to simulate charged particles in homogeneous turbulence. The governing equations and numerical implementation are presented in Sec. II. An overview of the PM, P^3M, and hybrid methods are then discussed in Sec. III and the accuracy of each are compared for a simple periodic box. The proposed EL P^3M method is then applied to a Taylor-Green vortex and homogeneous isotropic turbulence in Sec. IV to assess the competition between particle transport due to fluid coupling and Coulomb interactions. One-point and two-point statistics obtained using the PM and P^3M methods are compared to assess the effect of added accuracy on collision rate and clustering.

II. FLUID-PARTICLE DESCRIPTION

A. Governing equations

The flow of spherical particles suspended in a turbulent carrier phase is solved in an Eulerian-Lagrangian framework, where particles are treated as discrete entities of finite size and mass, and the gas phase is solved on a background Eulerian mesh. Due to the low concentrations considered in this study, volume fraction effects and two-way coupling between the phases are neglected. The governing equations for the incompressible carrier phase are given by

$$\nabla \cdot \boldsymbol{u}_f = 0 \tag{1}$$

and

$$\frac{\partial \boldsymbol{u}_f}{\partial t} + \boldsymbol{u}_f \cdot \nabla \boldsymbol{u}_f = -\frac{1}{\rho_f}\nabla p + \nu \nabla^2 \boldsymbol{u}_f, \tag{2}$$

where $\boldsymbol{u}_f = [u_f, v_f, w_f]^\mathsf{T}$ is the fluid velocity, ρ_f is the fluid density, and p and ν are the hydrodynamic pressure and kinematic viscosity, respectively.

The displacement of an individual particle i is calculated using Newton's second law of motion

$$\frac{d\boldsymbol{x}_p^{(i)}}{dt} = \boldsymbol{v}_p^{(i)} \tag{3}$$

and

$$m_p \frac{d\boldsymbol{v}_p^{(i)}}{dt} = \boldsymbol{F}_{\text{drag}}^{(i)} + \boldsymbol{F}_{\text{col}}^{(i)} + \boldsymbol{F}_{\text{Coulomb}}^{(i)}, \tag{4}$$

where $\boldsymbol{x}_p^{(i)}(t)$ and $\boldsymbol{v}_p^{(i)}(t)$ are the instantaneous particle position and velocity at time t, respectively, m_p is the particle mass, $\boldsymbol{F}_{\text{col}}^{(i)}$ is the collision force, and $\boldsymbol{F}_{\text{Coulomb}}^{(i)}$ is the electrostatic force. The classic Schiller-Naumann drag correlation [32] is used on the right-hand side of Eq. (4) to account for finite-Reynolds-number effects, given by

$$\frac{\boldsymbol{F}_{\text{drag}}^{(i)}}{m_p} = \frac{1 + 0.15\,\text{Re}_p^{0.687}}{\tau_p}\left(\boldsymbol{u}_f\left[\boldsymbol{x}_p^{(i)}\right] - \boldsymbol{v}_p^{(i)}\right), \tag{5}$$

where $\boldsymbol{u}_f[\boldsymbol{x}_p^{(i)}]$ is the fluid velocity at the location of particle i, $\text{Re}_p = \|\boldsymbol{u}_f[\boldsymbol{x}_p^{(i)}] - \boldsymbol{v}_p^{(i)}\| d_p/\nu$ is the particle Reynolds number, with d_p the particle diameter, and $\tau_p = \rho_p d_p^2/18\rho_f\nu$ is the particle response time.

Despite the low-volume fractions considered here, particle collisions are needed to prevent unphysical overlap that may arise due to the attractive electrostatic forces between oppositely charged particles. In this work, normal and tangential collisions are modeled using a modified soft-sphere approach [18] originally proposed by Cundall and Strack [33]. When two particles come into contact, a repulsive force is created as

$$\boldsymbol{f}_{n,j\to i}^{\text{col}} = \begin{cases} -k\delta_{ij}\boldsymbol{n}_{ij} - \eta \boldsymbol{v}_{ij,n} & \text{for } r_{ij} < 2d_p + \Lambda \\ 0 & \text{otherwise,} \end{cases} \tag{6}$$

where r_{ij} is the distance between the center of the particles, δ_{ij} is the overlap between the particles, and $\boldsymbol{n}_{ij} = \boldsymbol{r}_{ij}/|\boldsymbol{r}_{ij}|$ is the unit normal vector from particle i to particle j with $\boldsymbol{r}_{ij} = \boldsymbol{x}_p^{(j)} - \boldsymbol{x}_p^{(i)}$. The normal relative velocity between particles i and j is given by

$$\boldsymbol{v}_{ij,n} = \left[\left(\boldsymbol{v}_p^{(i)} - \boldsymbol{v}_p^{(j)}\right) \cdot \boldsymbol{n}_{ij}\right]\boldsymbol{n}_{ij}. \tag{7}$$

The spring stiffness and damping parameter are given by k and η, respectively. A model for the damping parameter [33] uses a coefficient of restitution $0 < e < 1$ such that

$$\eta = -2 \ln e \frac{\sqrt{k m_p/2}}{\sqrt{\pi^2 + (\ln e)^2}}. \tag{8}$$

The spring stiffness is related to the collision time τ_{col} according to

$$k = m_p/2\tau_{\text{col}}^2[\pi^2 + (\ln e)^2]. \tag{9}$$

In the present study, we consider inelastic collisions with a coefficient of restitution $e = 0.9$, representative of many solid spherical objects in dry air. To properly resolve the collisions without requiring an excessively small time step, τ_{col} is set to be 15 times the simulation time step for all simulations presented in this work. In Eq. (6), Λ is set to a small number that allows for collisions to initiate before particles are in contact, which is adjusted dynamically such that slow moving particles make physical contact and high-speed collisions remain robust [18]. To account for friction between particles and thus particle rotation, the static friction model is employed for the tangential component of the collision force, given by

$$\boldsymbol{f}_{t,j\to i}^{\text{col}} = -\mu_f \left|\boldsymbol{f}_{n,j\to i}^{\text{col}}\right| \boldsymbol{t}_{ij}, \tag{10}$$

where $\mu_f = 0.1$ is the coefficient of friction and $\boldsymbol{t}_{ij} = \boldsymbol{v}_{ij,t}/|\boldsymbol{v}_{ij,t}|$ is the tangential unit vector. The tangential unit vector is defined as $\boldsymbol{v}_{ij,t} = \boldsymbol{v}_{ij} - \boldsymbol{v}_{ij,n}$, where $\boldsymbol{v}_{ij} = \boldsymbol{v}_p^{(j)} - \boldsymbol{v}_p^{(i)}$ is the relative velocity between particles i and j. Once each individual collision force is computed, the full collision force that particle i experiences can be expressed as

$$\boldsymbol{F}_{\text{col}}^{(i)} = \sum_{j\neq i} \left(\boldsymbol{f}_{n,j\to i}^{\text{col}} + \boldsymbol{f}_{t,j\to i}^{\text{col}}\right). \tag{11}$$

Finally, the angular velocity of particle i, $\boldsymbol{\omega}_p^{(i)}$, is constructed using Eq. (10) by

$$I_p \frac{d\boldsymbol{\omega}_p^{(i)}}{dt} = \sum_j \frac{d_p}{2} \boldsymbol{n}_{ij} \times \boldsymbol{f}_{t,j\to i}^{\text{col}}, \tag{12}$$

where $I_p = m_p d_p^2/10$ is the moment of inertia for a sphere.

The last term in Eq. (4) is the electrostatic force governed by Coulomb's law, given by

$$\boldsymbol{F}_{\text{Coulomb}}^{(i)} = \frac{q_p^{(i)}}{4\pi\epsilon_0} \sum_{j\neq i} q_p^{(j)} \frac{\boldsymbol{n}_{ij}}{\left|\boldsymbol{x}_p^{(j)} - \boldsymbol{x}_p^{(i)}\right|^2}, \tag{13}$$

where $q_p^{(i)}$ and $q_p^{(j)}$ are the charges belonging to particles i and j, respectively, and $\epsilon_0 = 8.854 \times 10^{-12}\ \text{F m}^{-1}$ is the vacuum permittivity. For the simulations considered in this work, the electrical permittivity is assumed constant and taken to be ϵ_0. The force of interaction between the particles is attractive if their charges have opposite signs and repulsive if like signed. As shown in Eq. (13), a direct summation will result in $O(N^2)$ computations. The following section will present various algorithms for computing this term with a focus on accuracy and efficiency. It should be noted that in real systems, each particle will contain a distribution of charges that evolve as they interact with each other. For example, tribocharging can generate large amounts of net positive or negative charge in charge-neutral systems for particles of the same dielectric material [34]. Because the EL framework

explicitly tracks the charge of each particle in addition to particle-particle contact, it is relatively straightforward to account for such effects. In the present work, however, these effects are neglected and particles are assumed to retain their charge throughout the duration of the simulation. Despite this, as particles agglomerate, the overall charge experienced by distant particles will correctly be neutral since opposite-signed charges in close proximity will have a cancellation effect when projected to the grid.

B. Numerical implementation

The equations are implemented in the framework of NGA [35], a fully conservative fluid solver tailored for turbulent flow computations. The Navier-Stokes equations are solved on a staggered grid with second-order spatial accuracy for both the convective and viscous terms and the second-order accurate semi-implicit Crank-Nicolson scheme of Pierce [36] is used for time advancement. The particles are distributed among the processors based on the underlying domain decomposition of the gas phase. A second-order Runge-Kutta scheme is used for updating each particle's position, velocity, and angular velocity. To avoid $O(N^2)$ calculations of the collision force, a nearest-neighbor detection algorithm is employed such that collisions are only considered between particles in adjacent grid cells [18]. Due to the long-range influence of $\boldsymbol{F}_{\text{Coulomb}}$ (i.e., its influence extends far beyond the adjacent grid spacing), the same cannot be done for electrostatic interactions. This will be addressed in the following section.

III. SOLUTION PROCEDURES FOR THE ELECTROSTATIC FORCE

A. Particle-mesh method

To avoid the $O(N^2)$ calculation involved with solving Eq. (13) via a direct summation, the PM method approximates the force according to

$$\boldsymbol{F}^{(i)}_{\text{Coulomb}} = q_p^{(i)} \boldsymbol{E}\big[\boldsymbol{x}_p^{(i)}\big], \tag{14}$$

where $\boldsymbol{E}[\boldsymbol{x}_p^{(i)}]$ is the electric field interpolated to the position of particle i. The electric field is obtained by taking the gradient of the electric potential via

$$\boldsymbol{E}(\boldsymbol{x},t) = -\nabla\phi(\boldsymbol{x},t), \tag{15}$$

where $\boldsymbol{x}$ is the Eulerian coordinate system and the electric potential ϕ is calculated by solving the Poisson equation

$$\nabla^2\phi(\boldsymbol{x},t) = -\frac{\rho_m(\boldsymbol{x},t)}{\epsilon_0}. \tag{16}$$

The charge density ρ_m is obtained by interpolating the particle charge using the convolution product

$$\rho_m(\boldsymbol{x},t) = \sum_{i=1}^{N_p} q_p^{(i)} \mathcal{W}\big(\boldsymbol{x} - \boldsymbol{x}_p^{(i)}(t)\big), \tag{17}$$

where $\mathcal{W}$ is a polynomial weighting function that projects the particle charge to the mesh and N_p is the number of particles. In the following sections, different orders of the weighting function will be considered to assess its effect on the overall order of accuracy.

B. Ewald summation

While the PM approach avoids $O(N^2)$ calculation, it requires that the length scale used to resolve the spatial gradients of electric potential is greater than the spacing between the particles. Due to nontrivial interactions between the phases in turbulent flows, particles may preferentially concentrate in certain regions and thus in general this assumption does not hold. Ewald summation separates

the long-range and short-range forces to efficiently compute the electrostatic force in periodic boxes with quick convergence. Consider a system of N_p particles with charges $q_p^{(i)}$ at positions $\boldsymbol{x}_p^{(i)}$ in a cubic box of length L with triply periodic boundary conditions. The Ewald summation approach separates the total force of particle i into three components

$$\boldsymbol{F}^{(i)}_{\text{Coulomb}} = \boldsymbol{F}^{(i)}_r + \boldsymbol{F}^{(i)}_k + \boldsymbol{F}^{(i)}_d, \tag{18}$$

where $\boldsymbol{F}^{(i)}_r$ and $\boldsymbol{F}^{(i)}_k$ represent contributions from real space and Fourier space, respectively, and $\boldsymbol{F}^{(i)}_d$ is the dipole correction term to avoid double counting. These separate contributions are expressed as

$$\boldsymbol{F}^{(i)}_r = q_p^{(i)} \sum_j q_p^{(j)} {\sum_{\boldsymbol{m}\in\boldsymbol{Z}^3}}' \left(\frac{2\alpha}{\sqrt{\pi}} \exp(-\alpha^2 |\boldsymbol{r}_{ij} + \boldsymbol{m}L|^2) + \frac{\operatorname{erfc}(\alpha|\boldsymbol{r}_{ij} + \boldsymbol{m}L|)}{|\boldsymbol{r}_{ij} + \boldsymbol{m}L|} \right) \frac{\boldsymbol{r}_{ij} + \boldsymbol{m}L}{|\boldsymbol{r}_{ij} + \boldsymbol{m}L|^2}, \tag{19}$$

$$\boldsymbol{F}^{(i)}_k = \frac{q_p^{(i)}}{L^3} \sum_j q_p^{(j)} \sum_{\boldsymbol{k}\neq 0} \frac{4\pi \boldsymbol{k}}{k^2} \exp\left(-\frac{k^2}{4\alpha^2} \right) \sin(\boldsymbol{k}\cdot\boldsymbol{r}_{ij}), \tag{20}$$

and

$$\boldsymbol{F}^{(i)}_d = -\frac{4\pi q_p^{(i)}}{(1+2\epsilon')L^3} \sum_j q_p^{(j)} \boldsymbol{x}_p^{(j)}, \tag{21}$$

where erfc is the complementary error function, $\boldsymbol{m}$ and $\boldsymbol{k}$ represent the number of iterations over periodic boxes in real and Fourier space, respectively, which are distinguished using a cutoff radius $r_{\max}$, and ϵ' is the dielectric constant, which in the case of a vacuum is $\epsilon' = 1$. The inverse length α, referred to as the Ewald parameter, tunes the relative weight of the real-space and the reciprocal-space contribution. Since long-range interactions converge significantly faster in Fourier space, the Ewald summation will converge after only a few iterations for both $\boldsymbol{m}$ and $\boldsymbol{k}$. As a result, the computational cost scales as $O(N^{3/2})$ with an optimal choice of α.

C. Particle-particle-particle–mesh method

While Ewald summation can provide an exact solution to electrically charged particles in periodic boxes, the computational cost is still relatively large as it scales like $O(N^{3/2})$. The P^{3}M method, introduced by Hockney and Eastwood [25], provides a faster way of computing the reciprocal-space contribution by replacing the Fourier transforms with a fast Fourier transform (FFT) [37] on an underlying mesh. The reciprocal contribution thus scales like $O(N \log N)$. With a well-chosen cutoff radius, it can be shown that the real-space contribution can be solved in $O(N)$, resulting in an overall computational cost of $O(N \log N)$.

Instead of using a point charge, the P^{3}M method reconstructs the charges by using a Gaussian charge distribution given by

$$G(\boldsymbol{r};\beta) = \frac{\beta^3}{\pi^{3/2}} e^{-\beta^2 r^2}, \tag{22}$$

whose Fourier transform can be easily obtained via

$$\hat{G}(\boldsymbol{k};\beta) = \int d^3r\, G(\boldsymbol{r};\beta) e^{-i\boldsymbol{k}\cdot\boldsymbol{r}} = e^{-k^2/(2\beta)^2}. \tag{23}$$

Here $\boldsymbol{k}$ is the wave number and the constant β tunes the standard deviation of the Gaussian distribution, commonly referred to as the P^{3}M constant, and $i = \sqrt{-1}$. Applying Gauss's law to Eq. (22), the resulting electric field located at the center of particle i is

$$\boldsymbol{E}^{(i)}_s = \sum_j \frac{q_p^{(j)} \boldsymbol{n}_{ij}}{2\epsilon_0 \pi^{3/2}} \left[\frac{\sqrt{\pi}}{2r_{ij}^2} \operatorname{erf}(r_{ij}\beta) - \frac{\beta}{r_{ij}} e^{-\beta^2 r_{ij}^2} \right]. \tag{24}$$

Since the field from a point particle and the field produced by the Gaussian function are both known analytically, the corrected short-range force can be expressed exactly as

$$\boldsymbol{F}_s^{(i)} = \begin{cases} \sum_j q_p^{(i)} q_p^{(j)} \left(\frac{\boldsymbol{n}_{ij}}{4\pi\epsilon_0 r_{ij}^2} - \frac{\boldsymbol{n}_{ij}}{2\epsilon_0 \pi^{3/2}} \left[\frac{\sqrt{\pi}}{2r_{ij}^2} \mathrm{erf}(r_{ij}\beta) - \frac{\beta}{r_{ij}} e^{-\beta^2 r_{ij}^2} \right] \right) & \text{for } r_{ij} < r_{\max} \\ 0 & \text{otherwise.} \end{cases} \tag{25}$$

The P^{3}M method handles the long-range force by sending the particle charge to the mesh and multiplying the resulting charge density by an influence function. This step optimizes the solution by minimizing the overall discretization error. The particle charges are first weighted to the underlying mesh to obtain the charge density $\rho_m(\boldsymbol{x})$. An FFT is then applied to transform the charge density to Fourier space $\hat{\rho}_m(\boldsymbol{k})$. The resulting charge density is convolved with the Gaussian screen function via

$$\hat{\rho}_l(\boldsymbol{k}) = \hat{\rho}_m(\boldsymbol{k}) \hat{G}(\boldsymbol{k}) \tag{26}$$

to obtain the screened density field. To minimize the force error introduced by the screen function $\hat{G}(\boldsymbol{k})$, we use the optimized influence function derived by Hockney and Eastwood [25] that replaces $\hat{G}(\boldsymbol{k})$ by

$$\hat{G}_{\mathrm{opt}}(\boldsymbol{k}) = \frac{\hat{\boldsymbol{D}}(\boldsymbol{k}) \cdot \sum_{\boldsymbol{m}\in\boldsymbol{Z}} \hat{U}^2\left(\boldsymbol{k} + \frac{2\pi}{\Delta x}\boldsymbol{m}\right) \hat{\boldsymbol{R}}^2\left(\boldsymbol{k} + \frac{2\pi}{\Delta x}\boldsymbol{m}\right)}{|\hat{\boldsymbol{D}}(\boldsymbol{k})|^2 \left[\sum_{\boldsymbol{m}\in\boldsymbol{Z}} \hat{U}^2\left(\boldsymbol{k} + \frac{2\pi}{\Delta x}\boldsymbol{m}\right) \right]^2}, \tag{27}$$

where

$$\hat{\boldsymbol{R}}(\boldsymbol{k}) = -i\boldsymbol{k} \frac{\hat{G}(\boldsymbol{k})}{k^2}, \tag{28}$$

$$\hat{U}(\boldsymbol{k}) = \left(\frac{\sin\frac{k_x \Delta x}{2}}{\frac{k_x \Delta x}{2}} \frac{\sin\frac{k_y \Delta x}{2}}{\frac{k_y \Delta x}{2}} \frac{\sin\frac{k_z \Delta x}{2}}{\frac{k_z \Delta x}{2}} \right)^{p+1}, \tag{29}$$

and

$$\hat{D}_j = \begin{cases} i \frac{\sin k_j \Delta x}{\Delta x} & \text{for finite differences} \\ i\boldsymbol{k} & \text{for spectral integration,} \end{cases} \tag{30}$$

with Δx being the mesh spacing that is assumed uniform in all directions. Next the potential field is calculated by solving the Poisson equation

$$k^2 \hat{\phi}_l(\boldsymbol{k}) = \frac{\hat{\rho}_l(\boldsymbol{k})}{\epsilon_0} \tag{31}$$

for $\hat{\phi}_l(\boldsymbol{k})$. An inverse Fourier transform is then applied to convert $\hat{\phi}_l(\boldsymbol{k})$ to real space $\phi(\boldsymbol{x})$. The electric field is then obtained by

$$\boldsymbol{E}_l(\boldsymbol{x},t) = -\nabla\phi(\boldsymbol{x},t) \tag{32}$$

on the mesh and interpolated to the particle position. Once the short-range field is calculated via Eq. (24), the total electric field can be obtained by

$$\boldsymbol{E}\left[\boldsymbol{x}_p^{(i)}\right] = \boldsymbol{E}_l\left[\boldsymbol{x}_p^{(i)}\right] + \boldsymbol{E}_s^{(i)}, \tag{33}$$

where $\boldsymbol{E}_l[\boldsymbol{x}_p^{(i)}]$ is the long-range electric field interpolated to the position of particle i. The total force can then be calculated via Eq. (14) and used to update the velocity of each particle.

D. Hybrid method

One drawback of the P^{3}M method is that it relies on Fourier transforms and therefore must be solved in periodic domains. While the present study is only concerned with periodic systems, many

applications involving suspensions of charged particles in turbulence are wall bounded. Kolehmainen *et al.* [31] recently proposed a hybrid method that combines the truncated pairwise summation approach for the short-range potential and an injection method for the long-range contribution. The electric field is given by

$$\boldsymbol{E}^{(i)}(\boldsymbol{x}_p) = \boldsymbol{E}_s^{(i)}(\boldsymbol{x}_p) + \boldsymbol{E}_l\left[\boldsymbol{x}_{\text{cell}}^{(i)}\right] + \boldsymbol{E}_c^{(i)}(\boldsymbol{x}_p), \tag{34}$$

where $\boldsymbol{E}_l[\boldsymbol{x}_{\text{cell}}^{(i)}]$ is the long-range electric force at $\boldsymbol{x}_{\text{cell}}^{(i)}$, the center of the cell that particle i belongs to. The short-range contribution is obtained by summing all pairwise electrostatic interactions within the cutoff radius,

$$\boldsymbol{E}_s^{(i)}(\boldsymbol{x}_p) = \frac{1}{4\pi\epsilon_0} \sum_{0<r_{ij}<r_{\max}} q_p^{(j)} \frac{\left(\boldsymbol{x}_p^{(i)} - \boldsymbol{x}_p^{(j)}\right)}{\left|\boldsymbol{x}_p^{(i)} - \boldsymbol{x}_p^{(j)}\right|^3}, \tag{35}$$

and the long-range contribution is found by

$$\boldsymbol{E}_l\left[\boldsymbol{x}_{\text{cell}}^{(i)}\right] = -\nabla\phi\left[\boldsymbol{x}_{\text{cell}}^{(i)}\right]. \tag{36}$$

Here the electric potential ϕ is obtained by solving a Poisson equation for the cell-averaged value via

$$\nabla^2\phi = -\frac{\rho_v}{\epsilon}, \tag{37}$$

with the cell-averaged charge density given by

$$\rho_v = \frac{1}{V_k} \sum_{\boldsymbol{x}_p^{(j)} \in V_k} q_p^{(i)}, \tag{38}$$

where V_k is the volume of the local cell that particle j belongs to. The final term $\boldsymbol{E}_c(\boldsymbol{x}_p^{(i)})$ is the contribution to be removed to avoid double counting, given by

$$\boldsymbol{E}_c^{(i)}(\boldsymbol{x}_p) = -\sum_{0<r_{ij}<r_{\max}} \begin{cases} 0 & \text{for } \boldsymbol{x}_p^{(i)} \text{ and } \boldsymbol{x}_p^{(j)} \text{ in the same cell} \\ \frac{1}{4\pi\epsilon} \frac{q_p^{(j)}\left(\boldsymbol{x}_{\text{cell}}^{(i)} - \boldsymbol{x}_{\text{cell}}^{(j)}\right)}{\left|\boldsymbol{x}_{\text{cell}}^{(i)} - \boldsymbol{x}_{\text{cell}}^{(j)}\right|^3} & \text{otherwise.} \end{cases} \tag{39}$$

While the hybrid method does not rely on the Fourier transform and thus can be applied to complex geometries, compared to the P^3M method, its accuracy is limited by the correction term that is of the order of the spatial discretization. For the P^3M method, however, the truncation error is compensated using an optimized influence function and thus its accuracy is expected to be significantly greater than the hybrid method.

IV. RESULTS AND DISCUSSION

A. Comparison of methods

Here we assess the accuracy of the PM, P^3M, and hybrid methods. We consider the system given by Deserno and Holm [24], where $N_p = 100$ oppositely charged particles (50 with positive unit charge and 50 negative) are randomly placed within a triply periodic box of length $L = 10$ m in the absence of a fluid. All cases are solved on a mesh of size $N = 32$ in each direction, with a cutoff radius $r_{\max} = 4$ m. The L_2-norm of the force error, given by

$$L_2 = \sqrt{\frac{1}{N_p} \sum_{i=1}^{N_p} \left(\boldsymbol{F}_{\text{Coulomb}}^{(i)} - \boldsymbol{F}_{\text{exact}}^{(i)}\right)^2}, \tag{40}$$

is shown in Fig. 1 as a function of the Ewald constant, where $\boldsymbol{F}_{\text{exact}}$ is the Coulomb force obtained from a well-converged Ewald summation. For comparison, the electric field is computed using both

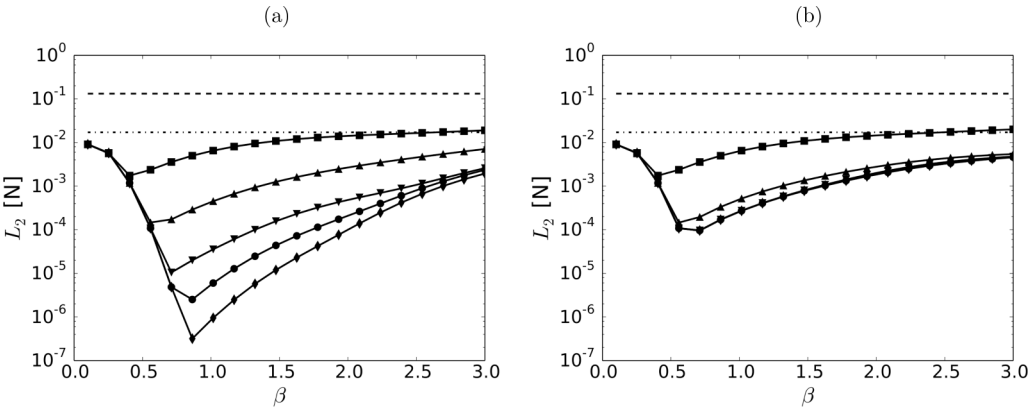

FIG. 1. Plot of the L_2-norm of the electrostatic force with the electric field computed as a function of the P^{3}M constant β that appears in Eq. (22) solved using (a) spectral difference and (b) finite difference for the PM method (——), the hybrid method (· · ·), and the P^{3}M method (symbols) with interpolation order 0 to 4 from top to bottom, respectively.

spectral-difference and finite-difference schemes. Results from the PM method were obtained by projecting the particle charge to the mesh and sending the resulting electric field to the particle location using second-order interpolation. It was found that changing the order of accuracy for interpolation when computing the PM had negligible effect on its L_2 error.

The P^{3}M method shows accuracy that is approximately five orders of magnitude higher than the PM and hybrid methods with a set of well-chosen parameters (i.e., in this case $\beta \approx 0.8$ and $r_{\max} = 4$ m). The hybrid method shows improvement over the PM method, though it does not outperform the P^{3}M method for the parameters under consideration for both the spectral- and finite-difference schemes. As shown in Fig. 1(b), when the electric field is evaluated via the finite difference, the errors associated with the P^{3}M method collapse for different orders of interpolation since the finite difference introduces truncation errors that cannot be eliminated by increasing the interpolation order. Since the P^{3}M method directly takes the differentiating scheme into account when constructing the optimized screen function $\hat{G}(\boldsymbol{k})$ in Eq. (30), increased accuracy is obtained when the spectral scheme is employed for the P^{3}M method. The PM and hybrid methods, however, do not show improvement when using spectral differences. In the remainder of this study, only second-order finite-difference operators will be considered when computing the gradient of the electric potential to be consistent with the difference operators employed in the EL framework as described in Sec. II B. Throughout the remainder of this paper, only the P^{3}M and PM methods will be considered to access the added benefits of capturing the short-range interactions.

B. Charged particles in a Taylor-Green vortex

The Taylor-Green vortex flow is investigated as an example of demonstrating the competition between particle transport due to fluid coupling and electrostatics and highlight the importance of computing the short-range interaction correctly. We consider a pseudo-two-dimensional flow field given by

$$\begin{aligned} u_f &= V_0 \cos\left(\frac{2\pi x}{L}\right) \sin\left(\frac{2\pi y}{L}\right), \\ v_f &= -V_0 \sin\left(\frac{2\pi x}{L}\right) \cos\left(\frac{2\pi y}{L}\right), \\ w_f &= 0 \end{aligned} \tag{41}$$

that remains constant throughout the simulation. Here the domain length L and characteristic velocity V_0 are chosen such that the Reynolds number $\mathrm{Re} = \rho_f V_0 L/\mu = 40$. It should be noted that the two-dimensional electric Poisson equation yields an electrostatic force that scales like $1/r$, which would require modifying the PM and P^{3}M formulations. To avoid this added complexity, a pseudo-two-dimensional domain is considered, discretized using $N = 32$ grid points in the x and y directions and four grid points in the z direction. Uniform grid spacing of L/N is employed in each direction. Particles are initially randomly distributed throughout the domain, half assigned with a positive charge and the other half a negative charge with a mean volume fraction $\langle \alpha_p \rangle = 1.0 \times 10^{-3}$. Different inertial regimes are considered by varying the Stokes number $\mathrm{St} = \tau_p/\tau_f$, where $\tau_f = L/V_0$ is the characteristic fluid time scale. For uncharged flows with a Stokes number below a critical value $\mathrm{St_{cr}} = 1/8\pi$, particles will closely follow fluid streamlines [38]. Above $\mathrm{St_{cr}}$, particle inertia is high enough such that they cross fluid streamlines, giving rise to particle-trajectory crossing [16]. For $\mathrm{St} = \mathrm{St_{cr}}$, particles will collapse between the vortices.

Following Karnik and Shrimpton [19], we introduce a dimensionless number v_c^* to characterize the relative magnitude of the electric field by first defining the electric settling velocity as

$$v_c = \tau_p \frac{E_{\mathrm{rms}}\,|q_p|}{m_p}, \tag{42}$$

where E_{rms} is the root-mean-square (rms) magnitude of the electric field and $|q_p|$ is the charge magnitude. The electric settling velocity represents the terminal velocity that a particle would attain due to the influence of a specified electric field in a quiescent flow. With this, the corresponding nondimensional electric settling velocity is

$$v_c^* = \frac{v_c}{u'}, \tag{43}$$

where u' is the rms fluid velocity magnitude.

Figures 2–4 show oppositely charged particles in the Taylor-Green vortex using the PM and P^{3}M as a function of v_c^* and St, with contours showing the vortex streamlines. The grayscale represents the self-induced electric-field magnitude resulting from fluid-particle coupling. In Fig. 2, the level of particle clustering can be seen to increase with increasing v_c^* with a more profound effect at low Stokes numbers. The uncharged case shows that particles are relatively homogeneously distributed for $\mathrm{St} = 0.1\,\mathrm{St_{cr}}$. Even as low as $v_c^* = 0.1$, Coulomb interactions are able to overcome fluid drag, causing particles to cross streamlines and organize into clusters. At $v_c^* = 1$ and $\mathrm{St} = 0.1\,\mathrm{St_{cr}}$, the clusters appear to be larger and chains of particles form and are advected within the Taylor-Green cells. As St approaches its critical value, increased inertia assists in the clustering process. Charged particles are found to agglomerate into chains between vortices even as low as $v_c^* = 0.1$. When $\mathrm{St} \gg \mathrm{St_{cr}}$, particles behave ballistically and require sufficient charge to cluster. In this case, clustering does not occur at $\mathrm{St} = 10\,\mathrm{St_{cr}}$ until $v_c^* = 1.0$. A zoomed-in view of the Taylor-Green flow is shown in Fig. 3. At early times ($t/\tau_p = 0.1$), long chains and rings form. The collision force plays an important role in restricting particles from overlapping as they form these complex structures. The attractive electrostatic force must overcome the rebound effect of colliding particles. Even with a coefficient of restitution of 0.9, the majority of contact is observed to result in stable structures. By the time the flow reaches a statistically stationary state, particles can be seen to self-organize into large agglomerates that accumulate in high-strain regions between vortices.

For comparison, the resulting particle distribution computed using the PM method is shown in Fig. 4. It can be seen that particle clustering is not able to be captured even at the highest charge density ($v_c^* = 1$) for the PM method, while particle agglomeration is present in all the P^{3}M cases. Because the direct pairwise sum is not accounted for in the PM method, short-range interactions are essentially averaged out when the charge is projected to the mesh. The complex structures observed in the P^{3}M calculations are thus unable to be captured. In the following section, a quantitative comparison between the P^{3}M and PM methods will be made in simulations of homogenous isotropic turbulence.

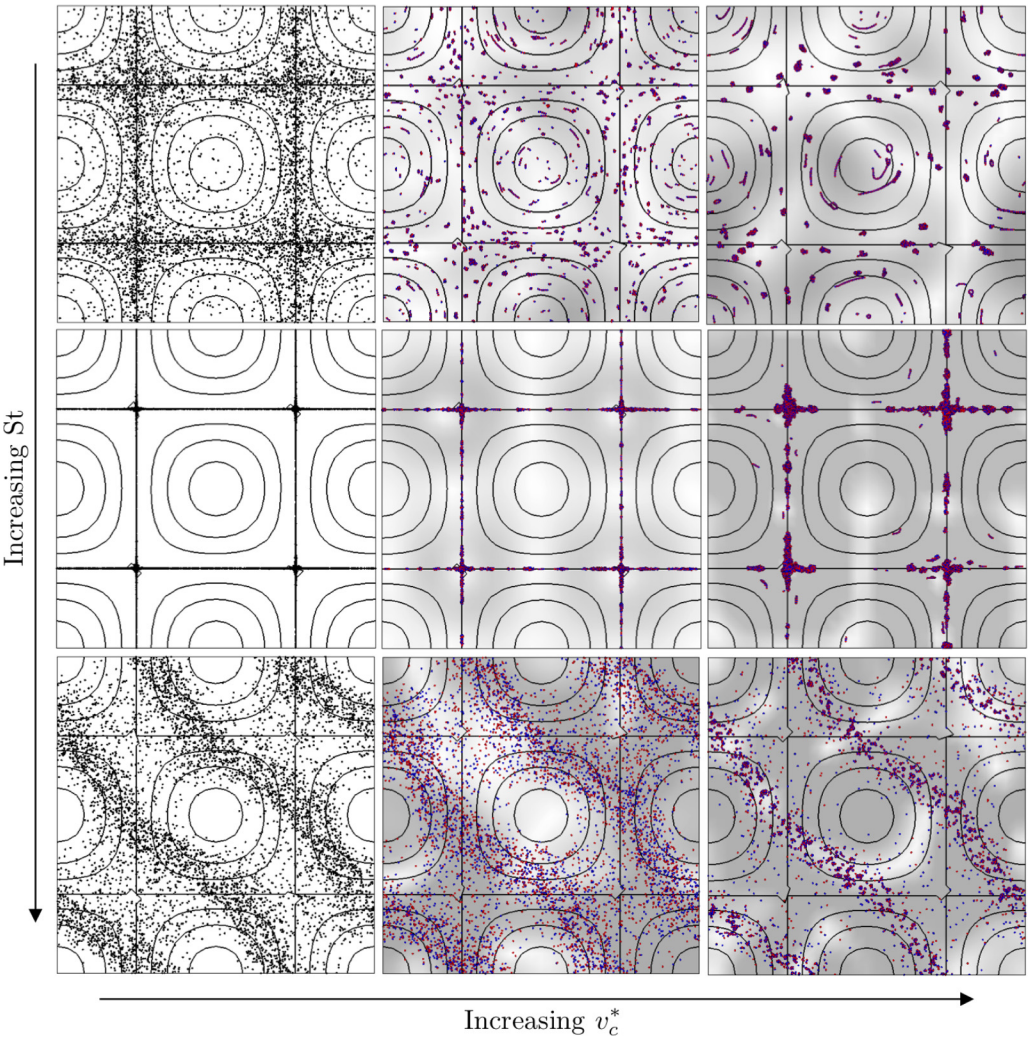

FIG. 2. Instantaneous particle position in the Taylor-Green vortex at $t/\tau_f = 1000$ using the P^{3}M method with increasing electric settling velocity $v_c^* = 0$, 0.1, and 1 (increasing from left to right) and $\mathrm{St}/\mathrm{St}_{\mathrm{cr}} = 0.1$, 1, and 100 (increasing from top to bottom). Grayscale represents the electric-field magnitude [ranging from 0 (white) to 10 000 V/m (black)]. Particles are colored by their charge: neutral (black), positive (red), and negative (blue).

C. Charged particles in homogeneous isotropic turbulence

1. System configuration

In this section, we consider 10^5 particles suspended in homogeneous isotropic turbulence (HIT) with density ratio $\rho_p/\rho_f = 1000$. The simulation domain is triply periodic with each side of length $L = 2\pi$ m. Particles are initially randomly distributed within the domain. We consider two scenarios: (i) suspensions of like-charged particles (i.e., all particles contain the same charge) and (ii) suspensions of oppositely charged particles such that half of the particles have each polarity. The Taylor Reynolds number varies between $\mathrm{Re}_\lambda = 25.8$ and 43.5 with $\mathrm{Re}_\lambda = u'\lambda/\nu$, where $\lambda = \sqrt{15\nu/\epsilon}\,u'$ is the Taylor microscale. The viscous dissipation rate ϵ and rms fluctuating velocity u' are averaged over the stationary period of the forced HIT. To achieve the desired Re_λ, the linear

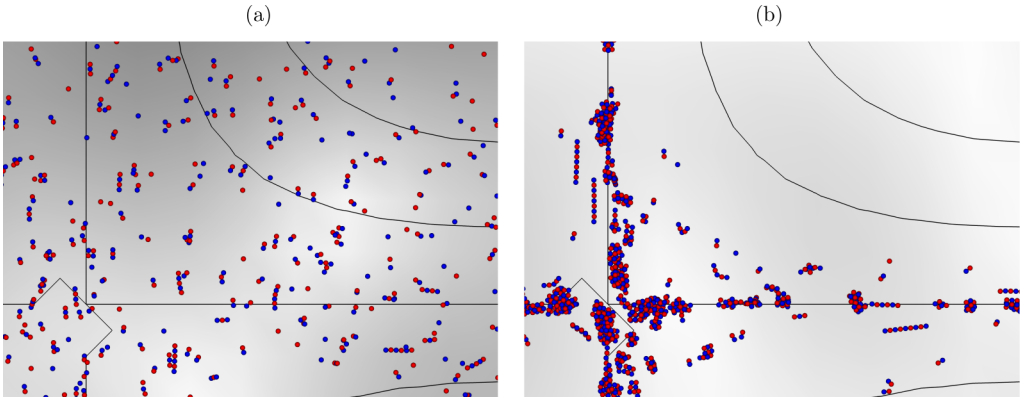

FIG. 3. Zoomed-in view of the Taylor-Green vortex computed using the P^{3}M method with $v_c^* = 0.1$, St = $\mathrm{St_{cr}}$, and (a) $t/\tau_f = 1$ and (b) $t/\tau_f = 10$. The color scheme is the same as in Fig. 2.

forcing scheme of Eswaran and Pope [39] is added to the right-hand side of Eq. (2). For each case, the particle diameter $d_p \ll \eta$, where $\eta = (\nu^3/\epsilon)^{1/4}$ is the Kolmogorov length scale, and the mean volume fraction $\langle \alpha_p \rangle \ll 1$ such that particles do not significantly modify the underlying turbulence and one-way coupling is applicable. In this work, angular brackets denote a volume average. Particle inertia is characterized by a turbulence Stokes number $\mathrm{St}_\eta = \tau_p/\tau_\eta$, where $\tau_\eta = (\nu/\epsilon)^{1/2}$ is the Kolmogorov time scale. The cutoff radius used in the P^{3}M method was chosen to be $r_{\max} = 4L/N$, with N the number of grid points in each direction. This was found to be the minimum value that was insensitive to the results reported herein. A list of relevant two-phase flow parameters used in each case is provided in Table I. These parameters correspond to 3.3- to 25-mm water droplets in air with charge $3 \times 10^{-9} < |q_p| < 60 \times 10^{-9}$ C. It should be noted that for cases with like charge, the Poisson equation used to solve the electric potential [Eq. (16) for the PM method and Eq. (31) for the P^{3}M method] is ill defined for the triply periodic system considered here. To that end, a uniform charge density is added to the background flow such that $\langle \rho_m \rangle = 0$.

2. *One-point statistics*

To quantify the degree of particle clustering, Eaton and Fessler [11] proposed to measure the deviation of volume fraction from a randomly distributed field of particles by defining a scalar parameter D as a measure for clustering, given by

$$D = \frac{\langle \alpha_p'^2 \rangle^{1/2} - \sigma_p}{\langle \alpha_p \rangle}, \tag{44}$$

where σ_p is the standard deviation of a corresponding flow with a random distribution of particles. The probability density function of volume fraction for the corresponding randomly distributed field is given by the discrete Poisson distribution, which is used to compute σ_p.

The parameter D is computed for each case and compared in Figs. 5 and 6. For the cases with like-charged particles, D follows the same trend as reported by Karnik and Shrimpton [19], that is, the level of clustering decreases with v_c^* for both the P^{3}M and PM methods. At low v_c^*, the Stokes number has a more significant effect on D, which is maximum at $\mathrm{St}_\eta = 1.0$ and decreases as St_η deviates from unity. As v_c^* increases, however, Coulomb interactions outcompete the drag force, causing the values of D to collapse with greater effect at lower Reynolds number. Little difference can be observed between the P^{3}M and PM methods in Fig. 5, suggesting that for the parameters under consideration, the repulsive Coulomb force is adequately captured without accounting for the direct pairwise sum.

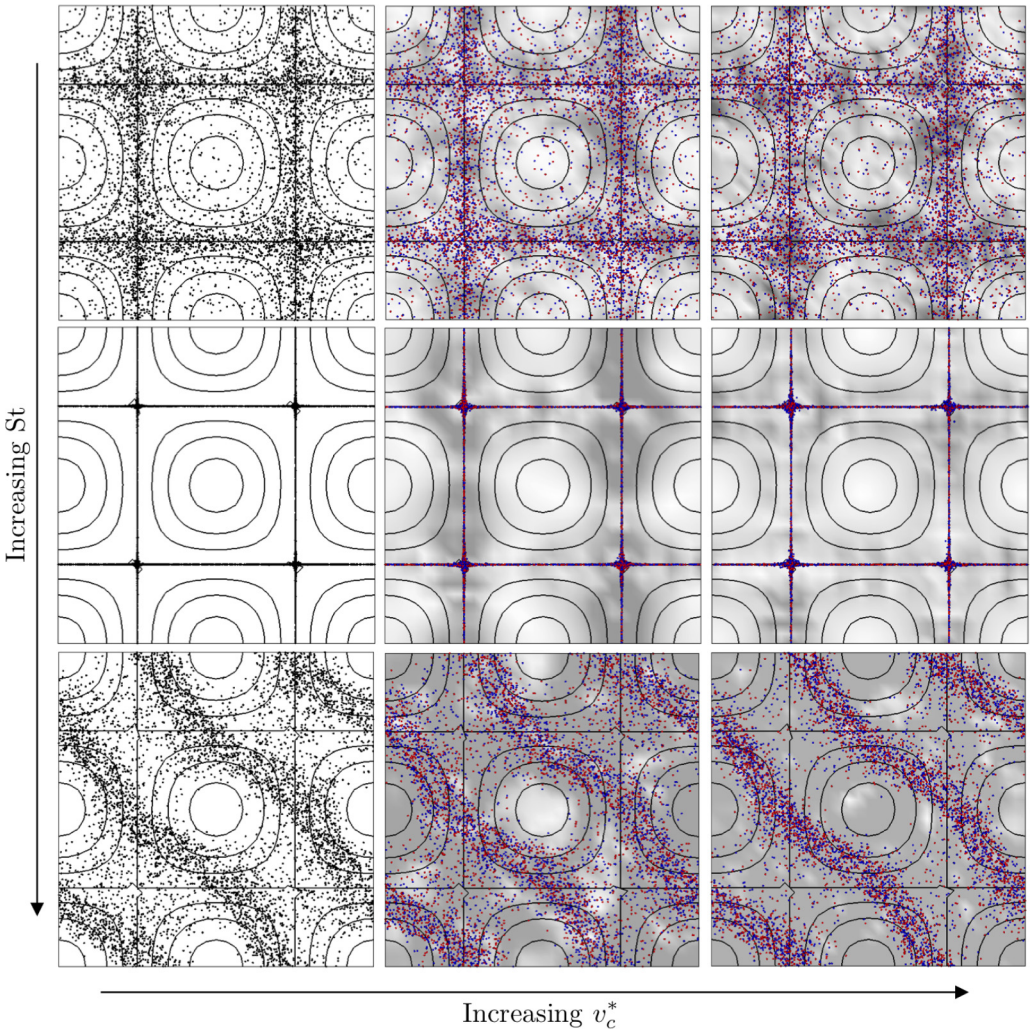

FIG. 4. Instantaneous particle position in the Taylor-Green vortex at $t/\tau_f = 1000$ using the PM method with increasing electric settling velocity $v_c^* = 0$, 0.1, and 1 (increasing from left to right) and $\mathrm{St}/\mathrm{St}_{\mathrm{cr}} = 0.1$, 1, and 100 (increasing from top to bottom). The color scheme is the same as in Fig. 2.

For cases with oppositely charged particles, however, the results of the PM and $\mathrm{P}^3\mathrm{M}$ methods deviate significantly, as shown in Fig. 6. Particles become highly clustered in the simulations computed using the $\mathrm{P}^3\mathrm{M}$ method since the short-range attractive force is accurately represented. For the simulations computed using the PM method, the level of clustering is not affected by the charge magnitude since the effect of opposite charges are essentially nullified when projecting the charge on the mesh. This discrepancy demonstrates the importance of correctly capturing the short-range interactions when particles contain opposite charges. In general, the level of clustering is maximum when $\mathrm{St}_\eta = 1.0$ and decreases as St_η increases. In Fig. 6(a), D varies from 0.72 to 2.84 when v_c^* increases from 0.25 to 0.5 for $\mathrm{Re}_\lambda = 25.8$. At higher Re_λ, however, the level of clustering is not as large due to increased velocity fluctuations causing local drag to overcome the attractive Coulomb forces. A similar effect is seen with variations in v_c^*. In Fig. 6(a), D increases by a factor of 4 when v_c^* changes from 0.25 to 0.5 for $\mathrm{Re}_\lambda = 25.8$, but only increases by a factor of 2 for $\mathrm{Re}_\lambda = 43.5$.

TABLE I. Parameters used in the HIT simulations.

N^3	Re_λ	St_η	$\langle\alpha_p\rangle$	d_p/η
32^3	25.8	0.48	7.86×10^{-5}	0.09
32^3	25.8	0.96	2.22×10^{-4}	0.12
32^3	25.8	6.16	3.63×10^{-3}	0.31
32^3	25.8	24.65	2.89×10^{-2}	0.62
64^3	43.5	0.44	7.56×10^{-6}	0.09
64^3	43.5	0.89	2.14×10^{-5}	0.13
64^3	43.5	7.02	4.85×10^{-4}	0.35
64^3	43.5	27.87	3.84×10^{-3}	0.70

3. Two-point statistics

Another important statistical measure of the spatial distribution of particles is the radial distribution function (RDF), defined as the number of particle pairs found at a given separation normalized by the expected number of pairs found in a homogeneous distribution [40]. The RDF $g(r)$ is calculated by binning particle pairs according to their separation distances within annular shells of thickness

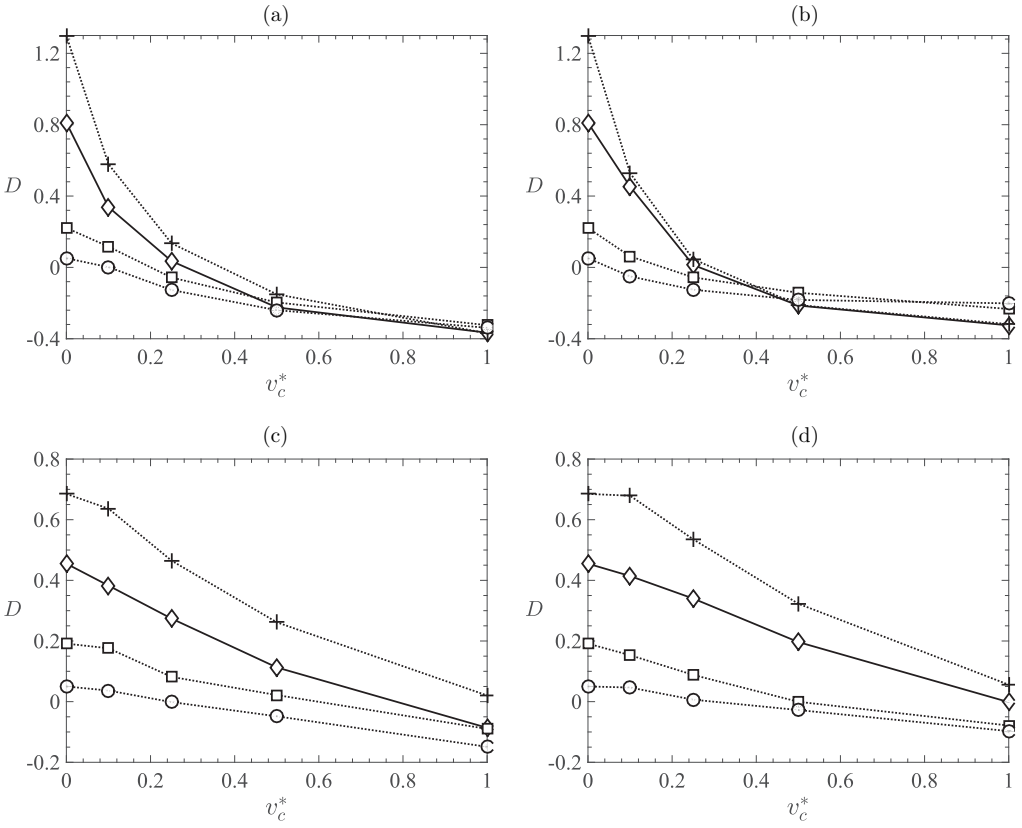

FIG. 5. Variation of D with nondimensional Coulomb velocity for $\mathrm{St}_\eta = 0.5$ (◇), 0.9 (+), 1.0 (+), 6.2 (□), 7.0 (□), 25.0 (◯), and 28.0 (◯) with like-charged particles for (a) $\mathrm{Re}_\lambda = 25.8$ ($\mathrm{P^3M}$ method), (b) $\mathrm{Re}_\lambda = 25.8$ (PM method), (c) $\mathrm{Re}_\lambda = 43.5$ ($\mathrm{P^3M}$ method), and (d) $\mathrm{Re}_\lambda = 43.5$ (PM method).

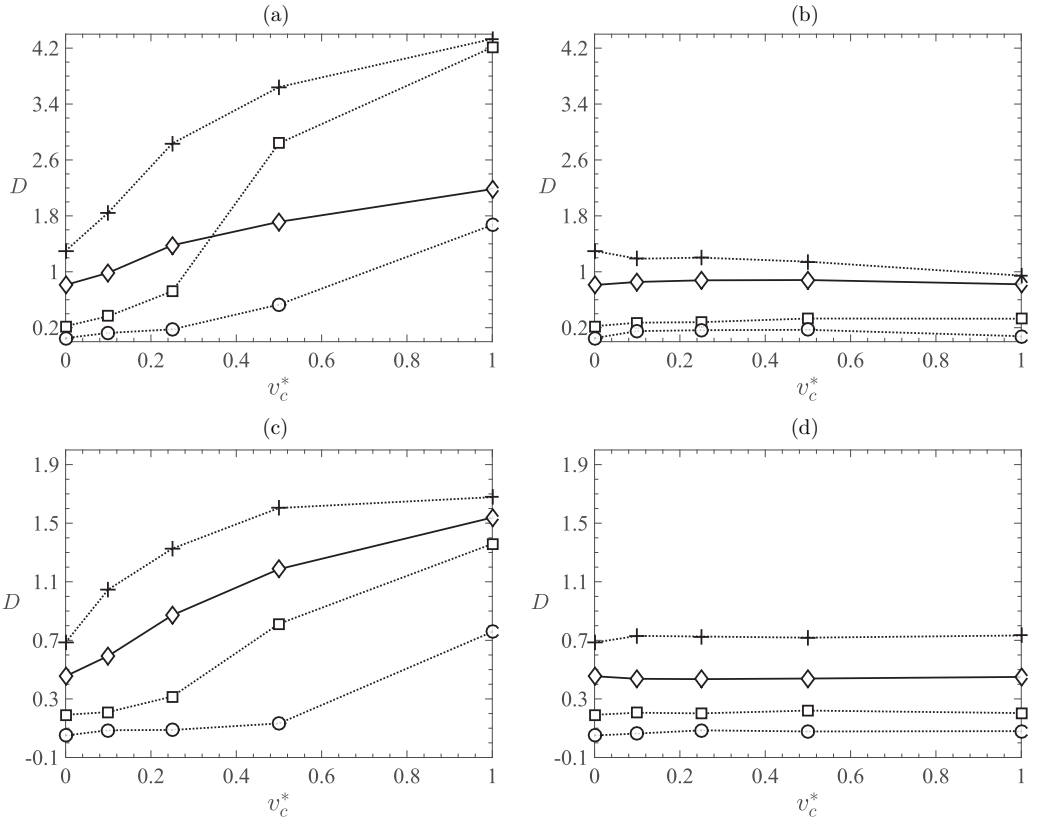

FIG. 6. Variation of D with nondimensional Coulomb velocity for $\mathrm{St}_\eta = 0.5$ (◇), 0.9 (+), 1.0 (+), 6.2 (□), 7.0 (□), 25.0 (◯), and 28.0 (◯) with oppositely charged particles for (a) $\mathrm{Re}_\lambda = 25.8$ ($\mathrm{P^3M}$ method), (b) $\mathrm{Re}_\lambda = 25.8$ (PM method), (c) $\mathrm{Re}_\lambda = 43.5$ ($\mathrm{P^3M}$ method), and (d) $\mathrm{Re}_\lambda = 43.5$ (PM method).

Δr, given by

$$g(r) = \frac{P_r/\Delta V_r}{P/V}, \tag{45}$$

where P_r is the number of particle pairs separated by a distance $r \pm \Delta r/2$, ΔV_r is the volume of the shell with thickness Δr located at separation r, $P = N_p(N_p - 1)/2$ is the total number of pairs in the simulation, and V is the volume of the sphere with radius $L/2$. With this definition, a value of unity represents a homogeneous distribution and values greater than unity imply clustering.

The RDFs are shown in Fig. 7 as a function of v_c^*. For the cases with like-charged particles, the presence of charge is seen to reduce the number of particle pairs up to a pair separation of 10η, which prevents particles from clustering. The result is consistent with what was shown in Fig. 5. In addition, for $r/\eta < 2$, the interparticle electrostatic repulsive force becomes extremely large and the RDF rapidly approaches zero. As for the case with oppositely charged particles, similar to what was observed in the like-charged cases, the RDF remains approximately close to unity for $2 < r/\eta < 10$. For $r/\eta < 2$, the RDF increases rapidly due to particle agglomeration. It was found that such short-range behavior of the two-point statistics was not observed when computed using the PM method.

The RDF can be seen to be greatly influenced by the Stokes number. Similar to what was observed in Figs. 5 and 6, the RDF is maximum when St_η is close to unity. With increasing v_c^*, the effect of charge for both like- and oppositely charged particles becomes more profound. Figure 8 shows the

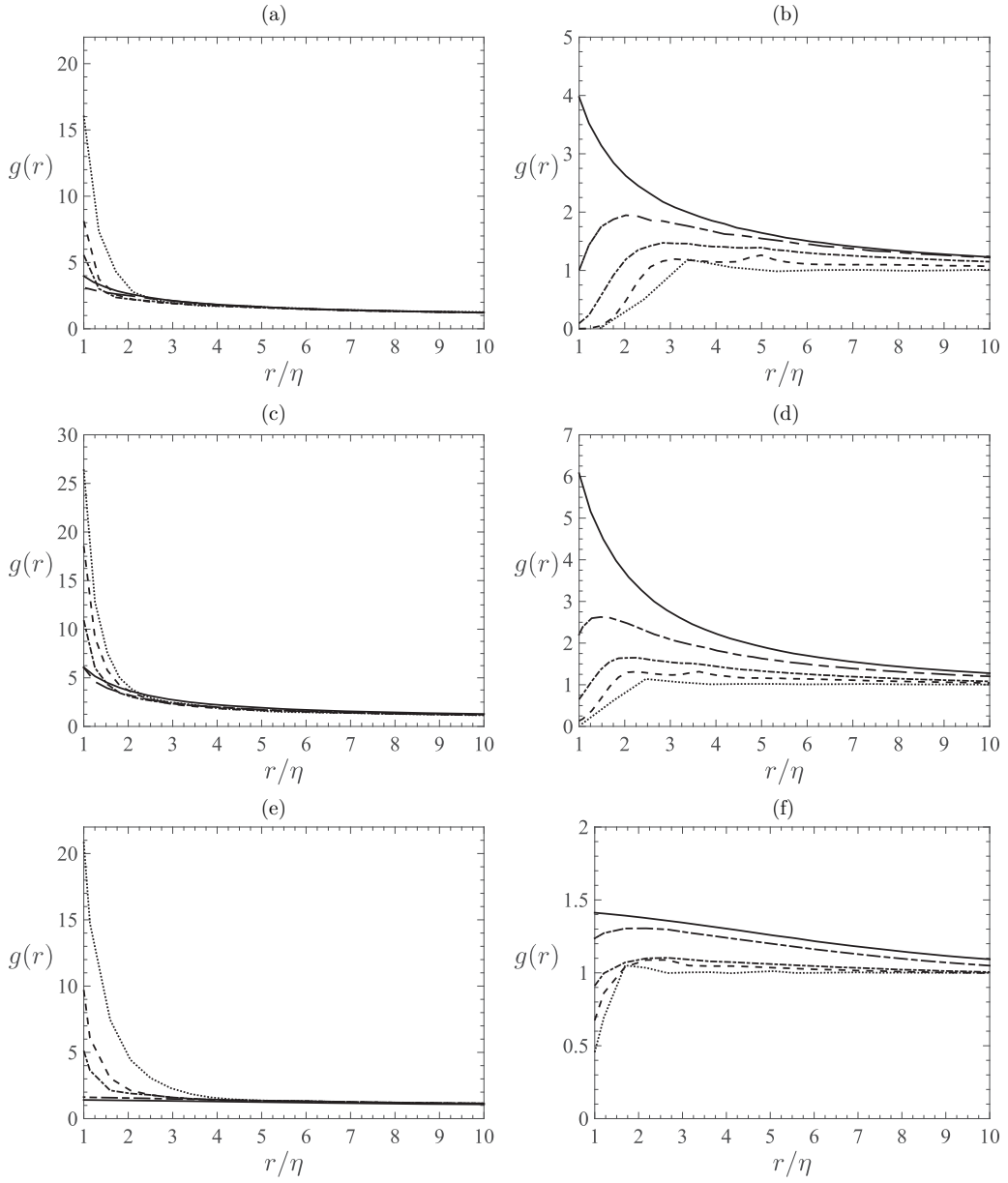

FIG. 7. Radial distribution functions for $\mathrm{Re}_\lambda = 43.5$ and (a) $\mathrm{St}_\eta = 0.5$, (b) $\mathrm{St}_\eta = 0.5$, (c) $\mathrm{St}_\eta = 1.0$, (d) $\mathrm{St}_\eta = 1.0$, (e) $\mathrm{St}_\eta = 7.0$, and (f) $\mathrm{St}_\eta = 7.0$ with $v_c^* = 0$ (−), 0.1 (— –), 0.25 (−·), 0.5 (−−), and 1.0 (· · ·) using the P^{3}M method, with (a), (c), and (e) oppositely charged particles and (b), (d), and (f) like-charged particles.

RDF in close contact as a function of St_η, defined as $g^* = g(1.5d_p)$. For oppositely charged particles, g^* is seen to increase with v_c^*, with a peak at $\mathrm{St}_\eta = 1$. Charges increase the peak of g^* by over an order of magnitude. For like-charged particles, an opposite trend is observed, with g^* decreasing as v_c^* increases, and the Stokes number is seen to play less of a role. For $\mathrm{St}_\eta \geqslant 7$, g^* approaches unity, suggesting that the Coulomb repulsive force has a greater influence than preferential concentration from drag and successfully homogenizes the suspension.

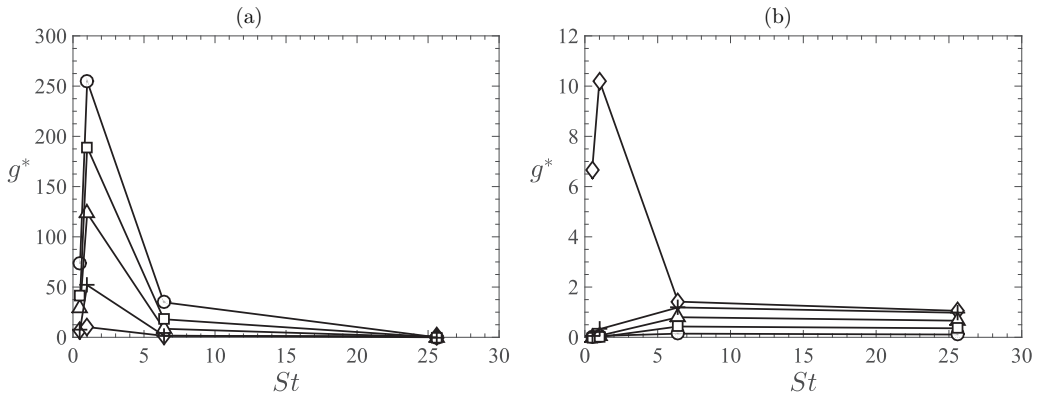

FIG. 8. The RDF near contact with $v_c^* = 0$ (◊), 0.1 (+), 0.25 (Δ), 0.5 (□), and 1.0 (◯) using the P^{3}M method, with (a) oppositely charged particles and (b) like-charged particles.

Lu and Shaw [20] recently proposed a model for the influence of charge on the RDF. Their model is based on the assumption that the particle relative velocity arises from dissipation-scale turbulent velocity fluctuations. The modeled RDF is a function of Stokes number and charge magnitude, though it is only valid for sufficiently weak charges such that the influence of Coulomb interactions is restricted to the dissipation scales of turbulence. Their model is able to capture increases in the RDF due to opposite charges and reductions in the RDF for like-charged particles, as was shown herein. However, the flow conditions are restricted to stagnant or low-St_η regimes. The charge density under consideration in their model was also several orders of magnitude smaller than what was used here and we found that it provides poor agreement with the RDFs reported here. This is to be expected, as St_η approaches unity, particle inertia has a stronger influence on the relative velocity between particles, and the fidelity of the model diminishes. Yet such models are necessary to provide accurate descriptions of the particle distribution without the burden of long simulation runtimes and the need for supercomputing resources. The method presented in this work can be used in future studies to improve upon such models.

V. SUMMARY AND CONCLUSIONS

In the present work, the role of electrostatic charge on particle clustering in turbulent flows was studied. The objective of this work was twofold: (i) present an accurate and tractable method for capturing electrically charged particles in turbulent flows and (ii) understand the interplay between fluid coupling (drag) and Coulomb interactions. Due to the long-range nature of the Coulomb potential, special attention was paid to treating the electrostatic force. We reviewed several methods, including the particle mesh, Ewald summation, particle-particle-particle–mesh, and hybrid approaches. We showed that the P^{3}M method admits several orders of magnitude higher accuracy for simple configurations of oppositely charged particles in periodic boxes. Both the PM and P^{3}M methods were implemented in an Euler-Lagrange framework that accounts for fluid-particle coupling and collisional contact between particles.

Results from simulations of a two-dimensional Taylor-Green vortex flow and three-dimensional homogeneous isotropic turbulence demonstrated that the Stokes number and electric charge play an important role in the particle dynamics. Despite the low-volume fractions considered here, interparticle collisions were found to be necessary to prevent unphysical overlap that arises via attractive Coulomb interactions. It was found that the PM method was capable of quantitatively capturing particle segregation for like-charged particles. However, the PM method was unable to capture particle chain and ring structures observed using the P^{3}M method for systems with oppositely charged particles.

The level of particle clustering in HIT was characterized via one- and two-point statistics. These measures were found to be highly influenced by the turbulence Stokes number St_η, Taylor Reynolds number Re_λ, and Coulomb settling velocity v_c^*. Similar to turbulent suspensions of uncharged particles, maximum clustering was observed when St_η approaches unity and decreased with values deviating from unity. In systems with oppositely charged particles, the level of clustering was seen to increase at larger values of Re_λ due to the increased influence of drag over the repulsive nature of the Coulomb interactions. The charge magnitude was found to play a dominating role in amplifying or suppressing the level of clustering. In suspensions of like-charged particles, the homogenization of particle distribution increased with increasing v_c^* for both the PM and $\mathrm{P}^3\mathrm{M}$ methods. However, the PM method was unable to capture enhanced particle segregation in systems with oppositely charged particles.

In real systems, neutral particles can acquire charge while highly charged particles may discharge themselves by capturing ions of the opposite polarity. Such effects were not considered in the present study. Instead, particles were assumed to retain their original charge throughout the duration of each simulation. Because the EL framework explicitly tracks the charge of each particle in addition to particle-particle contact, accounting for such effects can be implemented in a straightforward manner but might result in computationally restrictive time steps. Jin and Marshall [41] recently introduced a probabilistic model for contact electrification that presents a tractable approach to capture such effects.

Extending the EL $\mathrm{P}^3\mathrm{M}$ approach to arbitrary geometries will also require additional work. Ewald summation methods in general rely on Fourier transforms and are therefore restricted to periodic systems. Beams *et al.* [42] recently proposed a finite-element-based $\mathrm{P}^3\mathrm{M}$ method that constructs the screen potentials using polynomial bases. The long-range component of the potential can then be solved using standard multigrid methods as opposed to Fourier transforms. However, this leads to a more involved short-range calculation. An alternative approach would be to consider fast multipole methods (see, e.g., [43,44]) or treecode algorithms (see, e.g., [45]) to account for the electrostatic force. Despite the choice of method, we have demonstrated in the present work that treatment of the Coulomb potential, even in relatively dilute particle suspensions, must be accounted for accurately to correctly capture clustering and agglomeration in turbulent flows.

ACKNOWLEDGMENT

Our sincere thanks extend to Scott High (now at University of Illinois, Urbana-Champaign) for his help regarding the implementation of the $\mathrm{P}^3\mathrm{M}$ method.

[1] L. Zhou and B. A. Tinsley, Production of space charge at the boundaries of layer clouds, J. Geophys. Res. **112**, D11 (2007).

[2] G. Hendrickson, Electrostatics and gas phase fluidized bed polymerization reactor wall sheeting, Chem. Eng. Sci. **61**, 1041 (2006).

[3] R. G. Rokkam, R. O. Fox, and M. E. Muhle, Computational fluid dynamics and electrostatic modeling of polymerization fluidized-bed reactors, Powder Technol. **203**, 109 (2010).

[4] R. G. Rokkam, A. Sowinski, R. O. Fox, P. Mehrani, and M. E. Muhle, Computational and experimental study of electrostatics in gas-solid polymerization fluidized beds, Chem. Eng. Sci. **92**, 146 (2013).

[5] J. Bellan, A new approach to soot control in diesel engines by fuel-drop charging, Combust. Flame **51**, 117 (1983).

[6] J. Bellan and K. Harstad, Electrostatic dispersions and evaporation of clusters of drops of high-energy fuel for soot control, Symp. Int. Combust. **26**, 1713 (1996).

[7] J. S. Shrimpton and A. J. Yule, Characterisation of charged hydrocarbon sprays for application in combustion systems, Exp. Fluids **26**, 460 (1999).

[8] N. O. Renno, J. F. Kok, H. Kirkham, and S. Rogacki, A miniature sensor for electrical field measurements in dusty planetary atmospheres, J. Phys.: Conf. Ser. **142**, 012075 (2008).

[9] J. F. Kok and N. O. Renno, The effects of electric forces on dust lifting: Preliminary studies with a numerical model, J. Phys.: Conf. Ser. **142**, 012047 (2008).
[10] F. Esposito, R. Molinaro, C. I. Popa, C. Molfese, F. Cozzolino, L. Marty, K. Taj-Eddine, G. Di Achille, G. Franzese, S. Silvestro, and G. G. Ori, The role of the atmospheric electric field in the dust-lifting process, Geophys. Res. Lett. **43**, 5501 (2016).
[11] J. K. Eaton and J. R. Fessler, Preferential concentration of particles by turbulence, Int. J. Multiphase Flow **20**, 169 (1994).
[12] S. Sundaram and L. R. Collins, Collision statistics in an isotropic particle-laden turbulent suspension. Part 1. Direct numerical simulations, J. Fluid Mech. **335**, 75 (1997).
[13] T. B. Anderson and R. Jackson, Fluid mechanical description of fluidized beds. Equations of motion, Ind. Eng. Chem. Fundam. **6**, 527 (1967).
[14] D. Gidaspow, *Multiphase Flow and Fluidization: Continuum and Kinetic Theory Descriptions* (Academic, New York, 1994).
[15] D. Z. Zhang and A. Prosperetti, Averaged equations for inviscid disperse two-phase flow, J. Fluid Mech. **267**, 185 (1994).
[16] O. Desjardins, R. O. Fox, and P. Villedieu, A quadrature-based moment method for dilute fluid-particle flows, J. Comput. Phys. **227**, 2514 (2008).
[17] Y. Tsuji, T. Kawaguchi, and T. Tanaka, Discrete particle simulation of two-dimensional fluidized bed, Powder Technol. **77**, 79 (1993).
[18] J. Capecelatro and O. Desjardins, An Euler-Lagrange strategy for simulating particle-laden flows, J. Comput. Phys. **238**, 1 (2013).
[19] A. U. Karnik and J. S. Shrimpton, Mitigation of preferential concentration of small inertial particles in stationary isotropic turbulence using electrical and gravitational body forces, Phys. Fluids **24**, 073301 (2012).
[20] J. Lu and R. A. Shaw, Charged particle dynamics in turbulence: Theory and direct numerical simulations, Phys. Fluids **27**, 065111 (2015).
[21] P. P. Ewald, The calculation of optical and electrostatic grid potential, Ann. Phys. (Leipzig) **369**, 253 (1921).
[22] J. W. Perram, H. G. Petersen, and S. W. De Leeuw, An algorithm for the simulation of condensed matter which grows as the 3/2 power of the number of particles, Mol. Phys. **65**, 875 (1988).
[23] M. Deserno and C. Holm, How to mesh up Ewald sums. I. A theoretical and numerical comparison of various particle mesh routines, J. Chem. Phys. **109**, 7678 (1998).
[24] M. Deserno and C. Holm, How to mesh up Ewald sums. II. An accurate error estimate for the particle-particle-particle-mesh algorithm, J. Chem. Phys. **109**, 7694 (1998).
[25] R. W. Hockney and J. W. Eastwood, *Computer Simulation Using Particles* (CRC, Boca Raton, 1988).
[26] S. Aboud, D. Marreiro, M. Saraniti, and R. Eisenberg, A Poisson P^3M force field scheme for particle-based simulations of ionic liquids, J. Comput. Electron. **3**, 117 (2004).
[27] J. H. Walther, R. Jaffe, T. Halicioglu, and P. Koumoutsakos, *Proceedings of the Summer School Center for Turbulence Research* (NASA Ames/Stanford University, Stanford, 2000), p. 5.
[28] R. Gargallo, P. H. Hünenberger, F. X. Avilés, and B. Oliva, Molecular dynamics simulation of highly charged proteins: Comparison of the particle-particle particle-mesh and reaction field methods for the calculation of electrostatic interactions, Protein Sci. **12**, 2161 (2003).
[29] Y. Shan, J. L. Klepeis, M. P. Eastwood, R. O. Dror, and D. E. Shaw, Gaussian split Ewald: A fast Ewald mesh method for molecular simulation, J. Chem. Phys. **122**, 054101 (2005).
[30] H. Couchman, Mesh-refined P3M-A fast adaptive N-body algorithm, Astrophys. J. **368**, L23 (1991).
[31] J. Kolehmainen, A. Ozel, C. M. Boyce, and S. Sundaresan, A hybrid approach to computing electrostatic forces in fluidized beds of charged particles, AIChE J. **62**, 2282 (2016).
[32] R. Clift, J. R. Grace, and M. E. Weber, *Bubbles, Drops, and Particles* (Courier, North Chelmsford, 2005).
[33] P. A. Cundall and O. D. L. Strack, A discrete numerical model for granular assemblies, Geotechnique **29**, 47 (1979).
[34] V. Lee, S. R. Waitukaitis, M. Z. Miskin, and H. M. Jaeger, Direct observation of particle interactions and clustering in charged granular streams, Nat. Phys. **11**, 733 (2015).

[35] O. Desjardins, G. Blanquart, G. Balarac, and H. Pitsch, High order conservative finite difference scheme for variable density low Mach number turbulent flows, J. Comput. Phys. **227**, 7125 (2008).
[36] C. D. Pierce, Progress-variable approach for large-eddy simulation of turbulent combustion, Ph.D. thesis, Stanford University, 2001.
[37] W. H. Press, S. A. Teukolsky, W. T. Vetterling, and B. P. Flannery, *Numerical Recipes in C* (Cambridge University Press, Cambridge, 1992), Chap. 12 .
[38] M. Massot, in *Multiphase Reacting Flows: Modelling and Simulation*, edited by D. L. Marchisio and R. O. Fox (Springer, Wien, 2007), pp. 79–123.
[39] V. Eswaran and S. B. Pope, An examination of forcing in direct numerical simulations of turbulence, Comput. Fluids **16**, 257 (1988).
[40] D. A. McQuarrie, *Statistical Mechanics* (Harper & Row, New York, 1976).
[41] X. Jin and J. S. Marshall, The role of fluid turbulence on contact electrification of suspended particles, J. Electrostat. **87**, 217 (2017).
[42] N. N. Beams, L. N. Olson, and J. B. Freund, A finite element based P^3M method for N-body problems, SIAM J. Sci. Comput. **38**, A1538 (2016).
[43] H. Cheng, L. Greengard, and V. Rokhlin, A fast adaptive multipole algorithm in three dimensions, J. Comput. Phys. **155**, 468 (1999).
[44] J. Board and L. Schulten, The fast multipole algorithm, Comput. Sci. Eng. **2**, 76 (2000).
[45] P. Li, H. Johnston, and R. Krasny, A Cartesian treecode for screened Coulomb interactions, J. Comput. Phys. **228**, 3858 (2009).